International Journal of Thermofluids 26 (2025) 101069

Contents lists available at ScienceDirect

International Journal of Thermofluids

journal homepage: www.sciencedirect.com/journal/international-journal-of-thermofluids

Neural networking analysis of thermally magnetized mass transfer coefficient (MTC) for Carreau fluid flow: A comparative study

Khalil Ur Rehman [a,*], Wasfi Shatanawi [a,b,*], Zeeshan Asghar [a], A.R.M. Kasim [c,d]

[a] Department of Mathematics and Sciences, College of Humanities and Sciences, Prince Sultan University, Riyadh 11586, Saudi Arabia
[b] Department of Mathematics, Faculty of Science, The Hashemite University, P.O Box 330127, Zarqa 13133, Jordan
[c] Centre for Mathematical Science, Universiti Malaysia Pahang, 26300 Gambang, Malaysia
[d] Center for Research in Advanced Fluid and Process, Universiti Malaysia Pahang, Lebuhraya Tun Razak, Gambang, Kuantan, 26300, Pahang, Malaysia

ARTICLE INFO

Keywords:
Carreau fluid
Mass transfer
Chemical reaction
Neural networks
Lie symmetry
Shooting method

ABSTRACT

The non-Newtonian fluids are used in several operations, including the transportation of crude oil, drilling fluids, and hydraulic fracturing fluids. These fluids' flow characteristics can be described by the Carreau model, which helps with the planning and improvement of manufacturing and transportation procedures. Owing to such motivation we have considered the Carreau fluid flow subject to a magnetized flat surface with porosity, heat generation, temperature slip, chemical reaction, and velocity slip effects. The problem is formulated as coupled differential equations. For solution purposes, the order of equations is reduced by performing Lie symmetry analysis. The compact equations are further solved by the shooting method. The evaluation of the mass transfer coefficient for the Carreau fluid model is done by using an Artificial Intelligence based neural model. The Schmidt number, porosity, magnetic, Weissenberg number, and chemical reaction parameters are treated as inputs while the mass transfer rate is taken as output. Owing to 10 neurons in the hidden layer, the network is trained by the Levenberg-Marquardt algorithm. It is found that the mass transfer rate exhibits a direct relation with the Schmidt number and chemical reaction parameter. The magnitude of the Carreau concentration is perceived to be higher for non-porous surfaces when the chemical reaction parameter and Schmidt number exhibit positive change.

1. Introduction

For zero shear rate, the smooth transition subject to constant viscosity is observed for the Carreau fluid model in comparison with power law fluid when the power law index is less than unity. Owing to such properties researchers considered Carreau fluid flow in various configurations like the falling trends of particles in spherical shapes through a Carreau fluid was predicted by Macha et al. [1]. The applicability of this approach was demonstrated by constructing a comparison of falling velocity through experimental data recorded for the fall of lead balls, steel, and glass, in polymer solutions with varying shear-thinning and elasticity measures. Khellaf and Lauriat [2] investigated centrifugally driven convective flow in a vertical annulus having a revolving heated cylinder. The outer cylinder was cold, and the endplates were believed to be adiabatic. The Carreau-shifted constitutive equation was used to represent shear thinning viscosity. Computations were carried out for various flow parameters. The findings reveal that the shear thinning effect reduces friction at the spinning cylinder while increasing heat transmission across the gap. It was also demonstrated that a decrease in apparent viscosity can result in oscillatory flows. Macha et al. [3] examined the free fall of prisms and short cylinders in polymer solutions by means of the Carreau fluid model. The effect of particle form and liquid rheological behavior on particle terminal velocity was investigated. The terminal falling velocity was explored in this study. The suggested procedure's usefulness was demonstrated by excellent agreement for experimental and estimated terminal falling velocity data. Hsu et al. [4] investigated the Carreau model and the impact of important factors such as double-layer thickness, particle and cavity relative sizes, and particle location. Several intriguing occurrences were discovered. Like a northward oriented electric field, a particle's mobility owns a local maximum when it is in the middle of an enclosure. When gets close to the north pole of a hollow, its mobility displays a local minimum as its location changes. For the south pole, it travels opposite to the field. Near the north pole, the vortices (both clock and

* Corresponding author.
E-mail address: krehman@psu.edu.sa (K.U. Rehman).

https://doi.org/10.1016/j.ijft.2025.101069

Available online 8 January 2025
2666-2027/© 2025 The Author(s). Published by Elsevier Ltd. This is an open access article under the CC BY-NC-ND license (http://creativecommons.org/licenses/by-nc-nd/4.0/).

counter-clock-wise) were formed. Lee et al. [5] explored the border impact on electrophoresis. With a weak electric field and lower surface potential, the examined electrophoresis for particles of spherical shape. The Carreau model, which was widely used to describe shear-thinning polymeric fluids, was employed to mimic the fluid's non-Newtonian behavior. They demonstrate that, in general, shear thinning increases a particle's electrophoretic mobility. The greater the significance of this impact, the thinner the double layer, and, because the presence of the planar surface enhanced the shear-thinning effect, the closer a particle was to the flat surface, the greater its mobility. Between the gap of surface and particles, viscosity and shear rate change, with the particle surface having the highest shear rate and lowest viscosity. In the Carreau flow field, the approach for estimating the falling terminal velocity of particles was proposed by Siska et al. [6]. The approach was based on a modification of a previously discovered equation for the fall of particles that included the particle dynamic shape component. The suggested procedure's appropriateness was proven by an excellent match with the experiment. The velocity of both prisms and cylinders rooted in polymer solutions was evaluated in the experiments. Hsu et al. [7] explored the edge influence on particle mobility in a Carreau fluid. The implications of the system's essential characteristics on the drag coefficient and the accompanying flow field were explored for the power-law index, Carreau fluid's relaxation time constant, and particle length. They demonstrate that the boundary effect has a greater impact and drag coefficient than particle size and fluid characteristics. Ali and Hayat [8] proposed an analytical solution for the Carreau flow in an asymmetric channel with sinusoidal wall changes. To tackle the flow problem, a long wavelength approximation was used. The perturbation approach was used with a small Weissenberg number. The key topics covered were pumping, axial pressure gradients, and trapping aspects. The findings for the Carreau and Newtonian fluids were compared. Hsu et al. [9] studied the drag on the particle with spherical shape in Carreau fluid theoretically, using a free surface cell model for the Carreau number, Reynolds number, the power-law index, and the void fraction in the range. The effects of particle concentration, Carreau fluid type, and Re on drag coefficient were investigated. They demonstrate that the drag coefficient (dc) shows decline values for lower particle concentration and that the shear-thinning characteristic of the fluid enhances flow field reversal in the rear area of a sphere. An empirical relationship was developed that links the dc with the vacancy %, the composition of the Carreau fluid, and the Reynolds number. Shamekhi and Sadeghy [10] investigated numerically the lid-driven Carreau-Yasuda cavity flow. They merged the PIM mesh-free approach with the characteristic-based split-scheme. The flow profiles were reported at Re=1000. For Newtonian cases, the findings from our PIM-CBS-A technique correspond well with benchmark results that exist in the literature. Their numerical outcomes were also compatible with existing studies obtained using LSM, with the added benefit that PIM requires fewer "points" to reach the same level of precision. The Carreau-Yasuda model results show a considerable influence on a fluid's shear-thinning behavior. Hayat et al. [11] studied Carreau flow in a channel with a magnetic field and varied wave patterns. An induced magnetic field was used to conduct the flow analysis. The long wavelength method was used. They created mathematical formulas for the stream function and magnetic force. The phenomena of pressure increase and pumping were highlighted. De et al. [12] provided a novel version of the mathematical equation to study the lubricants with rheological behavior that follows the Carreau fluid model. The flow rate and shear stress findings obtained using a novel Reynolds-Carreau equation were exhibited and compared to those produced by previous studies. An advancement in the examination of the Carreau fluid model can be accessed in Refs. [13,14].

The study of the interaction between conducting fluids and electromagnetic events is known as magnetohydrodynamics, or MHD. The MHD flow is significant in many engineering and technological fields, including MHD flow meters, MHD pumps, and MHD power generation. Therefore, various studies were reported by considering MHD aspects in flow field like Ishak et al. [15] took into consideration MHD viscous flow over a surface. The flow equations were solved by finite difference scheme. They examined the flow characteristics for various values of the controlling parameters. Along with the velocity and temperature profiles, numerical data were obtained for surfaces quantities. Turkyilmazoglu [16] demonstrated the continuous MHD flow on rotating disk. The Joule heating and viscous dissipation factors are taken into consideration. The effects of a rotation parameter were investigated using an extremely precise spectral numerical integration approach. Uddin et al. [17] offered the study on mass transfer for magnetized flow along porous surface. They assumed that the fluid was dense and incompressible, and they applied a homogeneous magnetic field normal to the flow. The reduced equations were then numerically solved using the Runge-Kutta sixth-order integration method in conjunction with the Nachtsheim-Swigert shot iteration technique. For varying values of the parameters, the behavior of flow field was examined. The findings were graphically shown and then examined.

According to Srikanth et al. [18], metal particle breakdown is a natural event, as is the chemical reaction of the metal particle with the solvent. Nevertheless, the fluid flow and viscosity are impacted by this breakdown. The nanofluid viscosity impact was addressed by the addition of the chemical reaction rate parameter in the formulation of viscosity provided. They noticed that a higher volume proportion of the solid resulted in more heat transmission. The breakdown of the metal particles reduced the heat transfer. Abbas et al. [19] offered chemically reactive flow field for Casson fluid with various physical effects. The solution was obtained by using bivariate spectral collocation approach. Following that, a graphic discussion was presented for flow factors, including temperature, concentration fields, and velocity. The Prandtl fluid on Riga surface with convective conditions and chemical reactions was carried out by Kumar et al. [20]. The RKF four-fifth approach was utilized to numerically solve the set of boundary layer equations that were converted. The obtained numerical results for the features of mass transfer and flow were analyzed for different physical parameters. For larger Schmidt numbers and chemical reaction parameters, the solutal boundary layer was noticed low. Krishna et al. [21] examined the chemical reaction aspects in Walter-B fluid near an oscillating porous plate with simultaneous heat and mass transfer. For small elastic parameter, the equations were solved by perturbation approach. With the aid of graphs, the formulas for the temperature, concentration, and velocity were obtained analytically. The behavior of the flow was also computationally examined in relation to various fluid parameters. The recent attempts in this direction can access in Refs. [22,23].

It is consensus among researchers that the Carreau fluid model is used to describe the rheological properties of non-Newtonian fluids. The model takes into account the shear rate dependence of the fluid's viscosity and can be used to describe a wide range of complex fluid behaviors in polymer melts, food processing, cosmetics, personal care products, the study of blood flow, Paints and coatings to mention just a few. Therefore owning to such motivation, we have used artificial intelligence (AI) to investigate the mass transfer aspects in the Carreau fluid model. The AI study of Carreau fluid flow with mass transfer at a flat surface, together with chemical reaction, externally imposed magnetic field, velocity slip, heat production, and thermal slip effects is not done yet. The key novelty of the present problem is itemized as follows:

- Formulation of Carreau fluid flows over a magnetized surface with pertinent physical effects.
- Lie symmetry procedure for the Carreau fluid flow narrating coupled differential equations

  How one can construct an Artificial Intelligence-based neural model to forecast the MTC up to a wide range of flow parameters?
- How MTC depends on Schmidt number and chemical reaction parameter ?
- What are the impacts of Schmidt number on Carreau flow field subject to a magnetized flat surface?

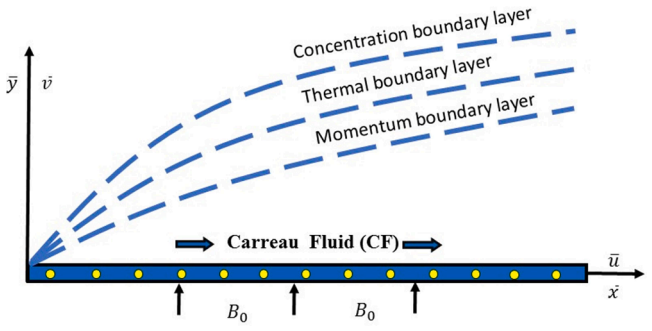

Fig. 1a. Geometry of problem.

- What are relations of chemical reaction with Carrea fluid concentration at porous/non-porous surfaces?

2. Flow formulation

The Carreau fluid flow is taken towards a flat surface. The externally applied magnetic field is considered normal to the flow. The mass and heat transfer aspects are taken in the presence of the following pertinent effects namely chemical reaction, thermal slip, velocity slip, and heat generation. The strength of both concentration and temperature are supposed higher at flat porous surfaces. The physical sketch of problem is given in Fig. 1(a). The relation of stress tensor for the Carreau fluid model is given as:

$$\overleftrightarrow{\tau} = -p\overleftrightarrow{\mathrm{I}} + \mu(\dot{\gamma}_c)\overleftrightarrow{A}_c, \tag{1}$$

here $\mu(\dot{\gamma}_c)$ is given as

$$\mu(\dot{\gamma}_c) = \mu_\infty + (\mu_0 - \mu_\infty)\left[1 + (\Gamma(t)\dot{\gamma}_c)^2\right]^{\frac{\lambda-1}{2}} \tag{2}$$

Considering $\mu_\infty = 0$, and $\Gamma(t)\dot{\gamma}_c < 1$, one can obtain

$$\overleftrightarrow{\tau} = -p\overleftrightarrow{\mathrm{I}} + \mu_0\left[1 + (\Gamma(t)\dot{\gamma}_c)^2\right]^{\frac{\lambda-1}{2}}\overleftrightarrow{A}_c. \tag{3}$$

Mathematical formulation subject to Carreau flow field in different scenario can be assessed in Refs. [24–28]. For the present flow problem, use of Eq. (3) results the following ultimate reduced equations are:

- Equation of continuity:

$$\bar{u}_{\bar{x}} + \bar{v}_{\bar{y}} = 0, \tag{4}$$

- Momentum equation

$$\bar{u}\bar{u}_{\bar{x}} + \bar{v}\bar{u}_{\bar{y}} = \nu_1\bar{u}_{\bar{y}\bar{y}} + \frac{\nu_1 3(\lambda-1)\Gamma(t)^2}{2}(\bar{u}_{\bar{y}})^2\bar{u}_{\bar{y}\bar{y}} - \frac{\mu}{\rho K_c}\bar{u} - \frac{\sigma {B_0}^2}{\rho}\bar{u}, \tag{5}$$

- Energy equation

$$\bar{u}\bar{T}_{\bar{x}} + \hat{v}\bar{T}_{\bar{y}} = (\kappa / c_p\rho)\bar{T}_{\bar{y}\bar{y}} + (Q_1 / c_p\rho)(\bar{T} - \bar{T}_\infty), \tag{6}$$

- Concentration equation

$$\bar{u}\bar{C}_{\bar{x}} + \bar{v}\bar{C}_{\bar{y}} = D_c\bar{C}_{\bar{y}\bar{y}} - k_m(\bar{C} - \bar{C}_\infty), \tag{7}$$

- Boundary conditions [29]

$$\bar{C} = \bar{C}_w\ ,\ \bar{T} = \bar{T}_w + D_1\bar{T}_{\bar{y}}\ \bar{v} = 0,\ \ \bar{u} = b\bar{x} + L_1\bar{u}_{\bar{y}},\ \ \text{at } \bar{y} = 0,$$
$$\bar{C}\to\bar{C}_\infty,\ \bar{u}\to 0,\ \bar{T}\to\bar{T}_\infty,\ \ \text{at } \bar{y}\to\infty. \tag{8}$$

It is important to note that p, μ, ρ, ν_1,σ, κ, c_p, D_c, $(\bar{u},\bar{v})$, $\bar{T}$and $\bar{C}$ represents the Pressure (N/m^2), fluid dynamic viscosity (N·s/m^2), fluid density (kg/m^3), kinematic viscosity (m^2/s), fluid electrical conductivity (S/m), thermal conductivity (W/m·K), specific heat at constant pressure (J/kg·K), mass diffusivity (m^2/s), velocities (m/s), temperature (K) and concentration (mol/L) respectively.

To have dimensionless form we used:

$$\phi = \frac{\bar{C} - \bar{C}_\infty}{\bar{C}_w - \bar{C}_\infty},\ \theta = \frac{\bar{T} - \bar{T}_\infty}{\bar{T}_w - \bar{T}_\infty},\ v = \frac{\bar{v}}{\sqrt{b\nu_1}},\ u = \frac{\bar{u}}{\sqrt{b\nu_1}},\ y = \sqrt{\frac{b}{\nu_1}}\bar{y},\ x = \sqrt{\frac{b}{\nu_1}}\bar{x}, \tag{9}$$

with the help of Eq. (9) we get

$$u_x + v_y = 0, \tag{10}$$

$$uu_x + vu_y = u_{yy} + \frac{3b(\lambda-1)\Gamma^2(t)}{2}u_{yy}(u_y)^2 - \frac{\mu}{\rho bK_c}u - \frac{\sigma {B_0}^2}{\rho b}u, \tag{11}$$

$$u\theta_x + v\theta_y = (\kappa / c_p\mu)\theta_{yy} + (Q_1 / c_p\rho b)\theta, \tag{12}$$

$$u\phi_x + v\phi_y = \frac{D_c}{\nu_1}\phi_{yy} - \frac{k_m}{b}\phi, \tag{13}$$

with BCs

$$\phi = 1,\ \theta = 1 + \sqrt{\frac{b}{\nu_1}}D_1\theta_y\ v = 0,\ u = x + \sqrt{\frac{b}{\nu_1}}L_1u_y, \qquad \text{for } y = 0,$$
$$\phi\to 0,\ \theta\to 0,\ u\to 0,\ \ \text{at } y\to\infty. \tag{14}$$

To get Lie symmetry transformation, we need the stream function relations for differential equations. Therefore, we own

$$v = -\Psi_x,\ u = \Psi_y, \tag{15}$$

hence:

$$\Psi_{xy} - \Psi_{yx} = 0, \tag{16}$$

$$\Psi_y\Psi_{xy} - \Psi_{y_y}\Psi_x = \Psi_{y_{y_y}} + \frac{3\Gamma(t)^2(\lambda-1)b}{2}\Psi_{y_{y_y}}\left(\Psi_{y_y}\right)^2 - \left(\frac{\mu}{\rho bK_c} + \frac{\sigma {B_0}^2}{\rho b}\right)\Psi_y, \tag{17}$$

$$\Psi_y\theta_x - \Psi_x\theta_y = (\kappa / c_p\mu)\theta_{yy} + (Q_1 / c_p\rho b)\theta, \tag{18}$$

$$\Psi_y\phi_x - \Psi_x\phi_y = \frac{D_c}{\nu_1}\phi_{yy} - \frac{k_m}{b}\phi, \tag{19}$$

with BCs

$$\phi = 1,\ \theta = 1 + \sqrt{\frac{b}{\nu_1}}D_1\theta_y\ \ \Psi_y = x + \sqrt{\frac{b}{\nu_1}}L_1\Psi_{yy},\ \ \Psi_x = 0, \qquad \text{for } y = 0,$$
$$\phi\to 0,\ \Psi_y\to 0,\ \theta\to 0,\ \text{when } y\to\infty. \tag{20}$$

3. Lie symmetry analysis

For a better description of the Carreau flow field, we constructed the scaling group of transformation rather than picking a random set of

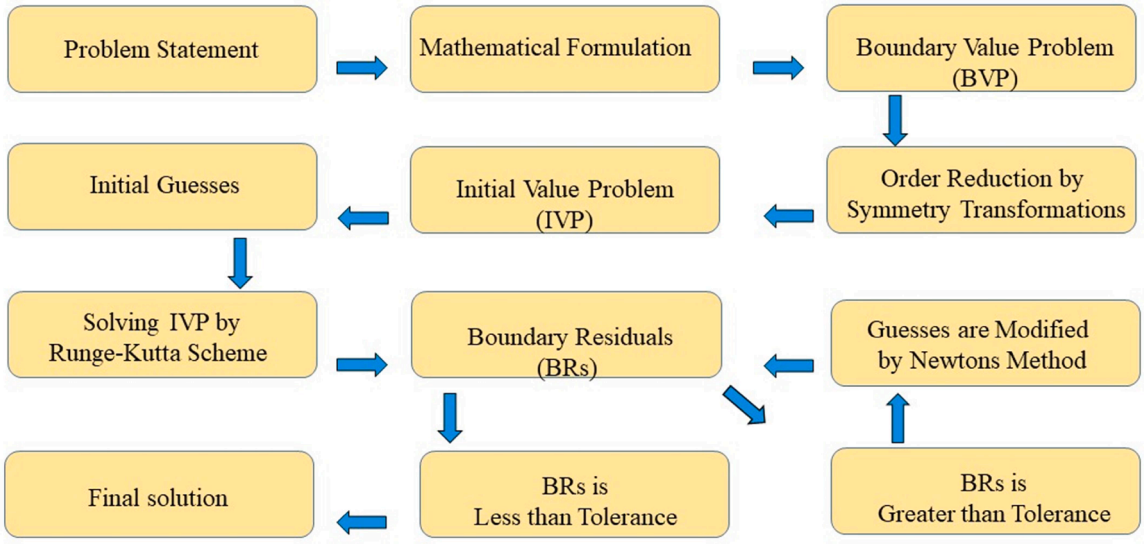

Fig. 1b. Flow chart of adopted shooting scheme.

transformations from the literature. For obtaining a set of symmetry transformations to reduce the order of Carreau flow equations we start with the following Lie group of transformation [29,30]:

$$L_T: \quad \phi^* = \phi e^{\varepsilon L_6},\ \Gamma^* = \Gamma(t) e^{\varepsilon L_5},\ \theta^* = \theta e^{\varepsilon L_4}, \Psi^* = \Psi e^{\varepsilon L_3},\ y_1 = y e^{\varepsilon L_2}, x_1 = x e^{\varepsilon L_1}. \tag{21}$$

By Eq. (18) we get

$$e^{\varepsilon(L_1+2L_2-2L_3)}\left(\Psi_{*y_1}\Psi_{*x_1y_1} - \Psi_{*x_1}\Psi_{*y_1y_1}\right) = e^{\varepsilon(3L_2-L_3)}\Psi_{*y_1y_1y_1} + e^{\varepsilon(7L_2-3L_3-2L_5)}\frac{3(\lambda-1)\Gamma_*^2 b}{2}\Psi_{*y_1y_1}\Psi_{*y_1y_1y_1} - e^{\varepsilon(L_2-L_3)}\left(\frac{\mu}{\rho b K_c} + \frac{\sigma B^2}{\rho b}\right)\Psi_{*y_1}, \tag{22}$$

$$e^{\varepsilon(L_1+L_2-L_3-L_4)}\left(\Psi_{*y_1}\theta_{*x_1} - \Psi_{*x_1}\theta_{*y_1}\right) = e^{\varepsilon(2L_2-L_4)}\left(\kappa/c_p\mu\right)\theta_{*y_1y_1} + e^{-\varepsilon L_4}\left(Q_1/c_p\rho b\right)\theta_*, \tag{23}$$

$$e^{\varepsilon(L_1+L_2-L_3-L_6)}\left(\Psi_{*y_1}\phi_{*x_1} - \Psi_{*x_1}\phi_{*y_1}\right) = e^{\varepsilon(2L_2-L_6)}\frac{D_c}{\nu_1}\phi_{*y_1y_1} - e^{-\varepsilon L_6}\frac{k_m}{b}\phi_*, \tag{24}$$

invariant condition for Eqs. (22–24) results

$$\begin{aligned} &3L_2 - L_3 = L_1 + 2L_2 - 2L_3 = L_2 - L_3 = 7L_2 - 3L_3 - 2L_5,\\ &2L_2 - L_4 = L_1 + L_2 - L_3 - L_4 = -L_4,\\ &2L_2 - L_6 = L_1 + L_2 - L_3 - L_6 = -L_6,\\ &L_4 = 0,\ L_6 = 0. \end{aligned} \tag{25}$$

Solving Eq. (25), we have

$$L_1 = L_1,\ L_2 = 0,\ L_3 = L_1,\ L_4 = 0,\ L_5 = -L_1 \text{ and } L_6 = 0. \tag{26}$$

Using Eq. (26) we get

$$L_T: \quad x_1 = x e^{\varepsilon L_1},\ \phi^* = \phi,\ \Gamma^* = \Gamma(t) e^{-\varepsilon L_1},\ \theta^* = \theta,\ \Psi^* = \Psi e^{\varepsilon L_1},\ y_1 = y. \tag{27}$$

alternatively:

$$\frac{d\phi}{0} = \frac{d\Gamma(t)}{-\Gamma(t)} = \frac{d\theta}{0} = \frac{d\Psi}{\Psi} = \frac{dy}{0} = \frac{dx}{x}. \tag{28}$$

hence

$$\phi = \phi_c(\eta_c),\ \Gamma(t) = x^{-1}\sqrt{\Gamma_0},\ \theta = \theta_c(\eta_c),\ \Psi = x f_c(\eta_c),\ \eta_c = y, \tag{29}$$

via Eq. (29) we have

$$\frac{d^3 f_c(\eta_c)}{d\eta_c^3} - \left(\frac{df_c(\eta_c)}{d\eta_c}\right)^2 + \frac{d^2 f_c(\eta_c)}{d\eta_c^2} f_c(\eta_c) + \frac{3(\lambda-1)}{2} W_c \frac{d^3 f_c(\eta_c)}{d\eta_c^3}\left(\frac{d^2 f_c(\eta_c)}{d\eta_c^2}\right)^2 - P_c\frac{df_c(\eta_c)}{d\eta_c} - {M_c}^2\frac{df_c(\eta_c)}{d\eta_c} = 0, \tag{30}$$

$$\frac{d^2\theta_c(\eta_c)}{d\eta_c^2} + \Pr\left(f_c(\eta_c)\frac{d\theta_c(\eta_c)}{d\eta_c}\right) + \Pr Q_c\,\theta_c(\eta_c) = 0, \tag{31}$$

$$\frac{d^2\phi(\eta_c)}{d\eta_c^2} + Sc\left(f_c(\eta_c)\frac{d\phi(\eta_c)}{d\eta_c}\right) - Sc\,Rm\,\phi(\eta_c) = 0, \tag{32}$$

with BCs

$$\phi(\eta_c) = 1\ f_c(\eta_c) = 0, \frac{df_c(\eta_c)}{d\eta_c} = 1 + a_1\frac{d^2 f_c(\eta_c)}{d\eta_c^2}, \theta(\eta_c) = 1 + \alpha_c\frac{d\theta(\eta_c)}{d\eta_c}, \text{at}\,\eta_c = 0,$$
$$\phi(\eta_c)\to 0,\ \theta(\eta_c)\to 0, \frac{df_c(\eta_c)}{d\eta_c}\to 0, \text{ when}\,\eta_c\to\infty. \tag{33}$$

Table 1
Effect of Sc on MTC for non-porosity case.

Sc	MTC
0.2	−0.2272
0.3	−0.2703
0.4	−0.3138
0.5	−0.3573
0.6	−0.4006
0.7	−0.4435
0.8	−0.4857
0.9	−0.5272
1.0	−0.5679
1.1	−0.6076
1.2	−0.6463
1.3	−0.6840
1.4	−0.7207
1.5	−0.7564
1.6	−0.7911
1.7	−0.8248
1.8	−0.8576
1.9	−0.8895
2.0	−0.9205

Table 2
Impact of Sc on MTC for porosity case.

Sc	MTC
0.2	−0.2136
0.3	−0.2504
0.4	−0.2880
0.5	−0.3262
0.6	−0.3649
0.7	−0.4038
0.8	−0.4429
0.9	−0.4819
1.0	−0.5207
1.1	−0.5591
1.2	−0.5971
1.3	−0.6345
1.4	−0.6713
1.5	−0.7074
1.6	−0.7426
1.7	−0.7771
1.8	−0.8108
1.9	−0.8437
2.0	−0.8757

Table 3
Effect of magnetic field parameter on MTC for non-porosity case.

M_c	MTC
0.05	−0.2717
0.10	−0.2358
0.15	−0.2348
0.20	−0.2336
0.25	−0.2697
0.30	−0.2689
0.35	−0.2274
0.40	−0.2246
0.45	−0.2215
0.50	−0.2179
0.55	−0.2141
0.60	−0.2618
0.65	−0.2604
0.70	−0.2590
0.75	−0.2575
0.80	−0.2561
0.82	−0.2555
0.85	−0.1860
0.90	−0.2531

Table 4
Impact of magnetic field parameter on Sherwood number for porosity case.

M_c	MTC
0.05	−0.2215
0.10	−0.2209
0.15	−0.2200
0.20	−0.2187
0.25	−0.2170
0.30	−0.2150
0.35	−0.2627
0.40	−0.2618
0.45	−0.2608
0.50	−0.2598
0.55	−0.2587
0.60	−0.2576
0.65	−0.2564
0.67	−0.2559
0.70	−0.2551
0.75	−0.1836
0.77	−0.2534
0.80	−0.2526
0.82	−0.2521

Table 5
Impact of chemical reaction on MTC for non-porosity case.

Rm	MTC
0.1	−0.2358
0.2	−0.2789
0.3	−0.3174
0.4	−0.3521
0.5	−0.3838
0.6	−0.4132
0.7	−0.4406
0.8	−0.4664
0.9	−0.4908
1.0	−0.5139
1.1	−0.5360
1.2	−0.5572
1.3	−0.5775
1.4	−0.5970
1.5	−0.6160
1.6	−0.6343
1.7	−0.6520
1.8	−0.6693
1.9	−0.6861

Table 6
Impact of chemical reaction on MTC for porosity case.

Rm	MTC
0.1	−0.2209
0.2	−0.2666
0.3	−0.3068
0.4	−0.3429
0.5	−0.3758
0.6	−0.4061
0.7	−0.4342
0.8	−0.4605
0.9	−0.4854
1.0	−0.5089
1.1	−0.5313
1.2	−0.5528
1.3	−0.5733
1.4	−0.5931
1.5	−0.6123
1.6	−0.6308
1.7	−0.6487
1.8	−0.6661
1.9	−0.6830

Table 7
Impact of Weissenberg number on MTC for porosity case.

W_c	MTC
0.05	−1.1310
0.10	−1.1314
0.15	−1.1317
0.20	−1.1929
0.25	−1.1931
0.30	−1.1934
0.35	−1.1936
0.40	−1.1939
0.45	−1.1941
0.50	−1.1943
0.55	−1.1945
0.60	−1.1349
0.65	−1.1353
0.70	−1.1356
0.75	−1.1359
0.80	−1.1363

Table 8
Effect of Weissenberg number on MTC for non-porosity case.

W_c	MTC
0.05	−1.1641
0.10	−1.1679
0.15	−1.1682
0.20	−1.1685
0.25	−1.1688
0.30	−1.2150
0.35	−1.2153
0.40	−1.2154
0.45	−1.2156
0.50	−1.2158
0.55	−1.2160
0.60	−1.2161
0.65	−1.2163
0.70	−1.2165
0.75	−1.2167
0.80	−1.2168

For Carreau fluid flow field, the ShD expression is:

$$ShD = \frac{\bar{x} q_m}{D_c(\bar{C}_w - \bar{C}_\infty)}, \quad q_m = -D_c \bar{C}_{\bar{y}}, \tag{34}$$

and ultimate form is

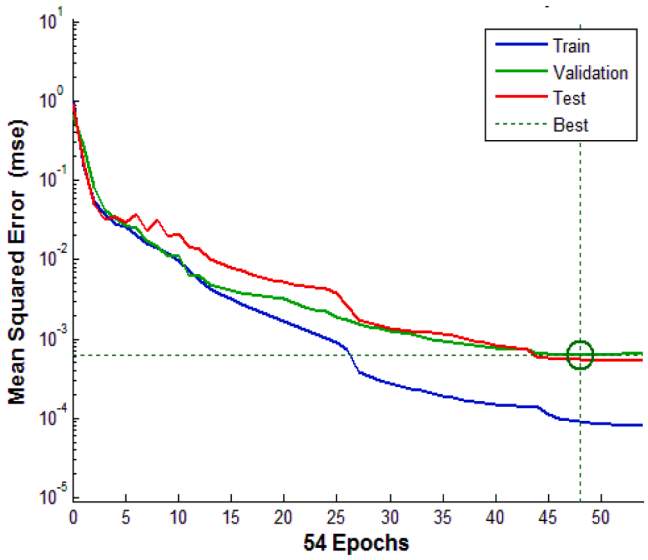

Fig. 2. Results of performance for the ANN model.

$$\frac{ShD}{\sqrt{\mathrm{Re}}} = -\frac{d\phi_c(0)}{d\eta_c}. \tag{35}$$

The flow parameters are

$$M_c = \sqrt{\frac{\sigma B^2}{\rho b}}, W_c = b\,\Gamma_0 \quad \mathrm{Pr} = \frac{\mu c_p}{\kappa}, \; Q_c = \frac{Q_1}{\rho c_p b}, \; P_c = \frac{\nu_1}{b K_c},$$
$$a_1 = \sqrt{\frac{b}{\nu_1}} L_1, \; \alpha_c = \sqrt{\frac{b}{\nu_1}} D_1, \; Sc = \frac{\nu_1}{D_c}, \; Rm = \frac{k_1}{b}. \tag{36}$$

We are interested in examining the mass transfer aspects which include concentration profile and Sherwood number at the porous surface when chemical reaction effects are considered in the concentration equation while heat generation and thermal slip effects are taken by means of energy equation for magnetized Carreau flow field.

For the solution purpose of flow equations, we used the Lie symmetry approach to construct the self-transformation rather than to use from available literature. The constructed transformations are used for order reduction of flow equations. Various techniques [31–34] exist to find the solution of fluid problems but in our problem, the shooting method [35, 36] is used for the solution of reduced equations. Shooting method is

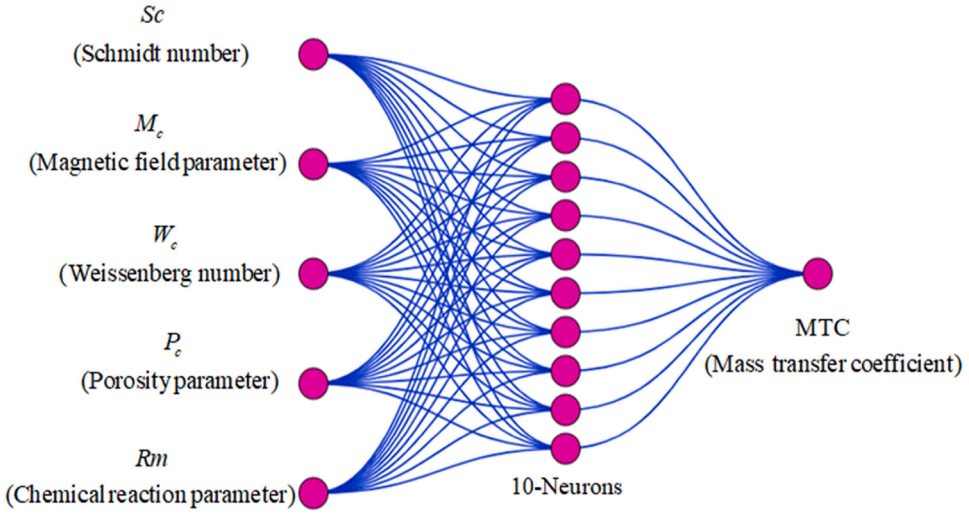

Fig. 1c. The neural network structure used to forecast MTC.

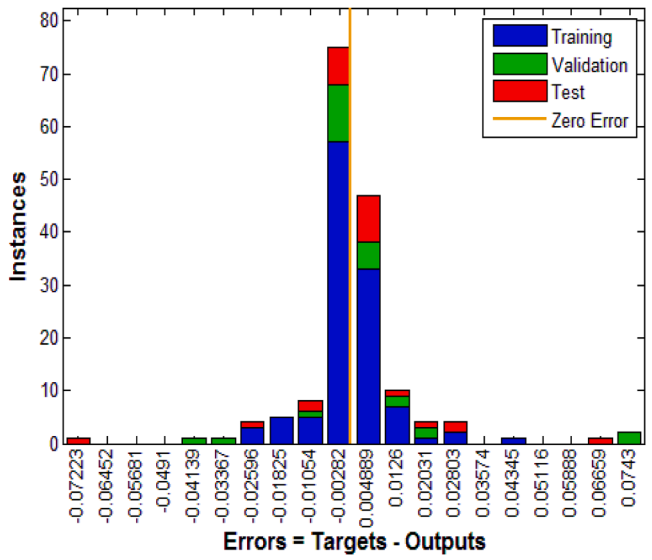

Fig. 3. ANN model histogram error plot.

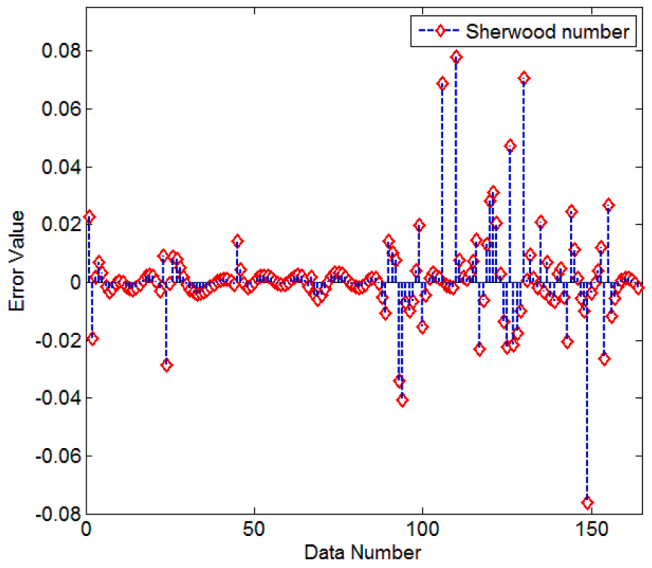

Fig. 4. Error outcome for ANN.

used to solve reduced system of first order differential.

The Runge-Kutta scheme is conjectured using Newtons Raphson method to find the numerical solution and the self-coding is carried in MATLAB-R2019a. The flow chart of shooting scheme is given in Fig. 1 (b). It is important to note that for all simulations CPU time ranges from 4 to 8 s.

4. Neural networking analysis

The Carreau fluid flow is mathematically formulated. With the assistance of Lie symmetry analysis, shooting method, and artificial intelligence, the solution is given. In detail, the mathematical formulation results in Schmidt number, velocity slip, Prandtl number, temperature slip, porosity, heat generation, magnetic field, chemical reaction parameters, and Weissenberg number. Our interest is to inspect the mass transfer features by using artificial intelligence for Carreau fluid flow

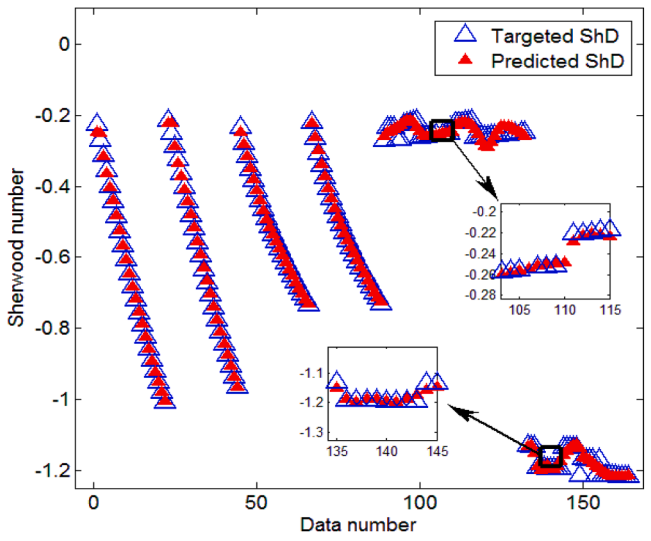

Fig. 5. A comparison plot for MTC values.

when heat transfer effects are present. The concentration equation holds Schmidt number and chemical reaction effects. The equation includes the momentum aspects as well therefore we own magnetic field parameter and porosity effects along Sc and reaction parameter to evaluate the Sherwood number and concentration profile. The shooting method is used to report the numerical data for MTC, see Tables 1–6. In detail, Table 1 gives the impact of Sc on Sherwood number at a non-porous surface. We witnessed that for higher values of Sc, the Sherwood number increased significantly.

The impact of Sc on Sherwood number for the case of the porous surface is noticed and shared by means of Table 2. It is seen that the Sherwood number shows inciting values for higher values of Sc number. The magnitude of the Sherwood number is greater for the Carreau fluid when the porosity effect is absent. For non-porous case, Table 3 demonstrates how M_c impacts ShD. We revealed that raising the magnetic field parameter reduces ShD. Important to note that the variation in ShD towards magnetic parameter shows a decline with a reversing trend like upto $M_c = 0.2$, it shows decline values and for $M_c = 0.25$ it jumps again to a higher value and later starts decreasing. Table 4 gives the impact of magnetic parameter on ShD for a porous case.

For increasing magnetic parameter, the ShD produces lower values with the same trend as in the case of the absence of porosity. Table 5 shows the influence of *Rm* on ShD in the absence of porosity. We can see that when the *Rm* grows, so do the ShD values. For the porosity case, Table 6 shows the variation in ShD towards larger Rm values. ShD is shown to grow when *Rm* increases. We observed that in the absence of porosity impact, the ShD seems to be somewhat stronger. Table 7 offers the Weissenberg number impact on MTC for both the porosity case. For higher values of Weissenberg number, the MTC get increased to value $W_c = 0.55$and for the increment up-to $W_c = 0.8$, it shows opposite trend. Table 8 depicts the Weissenberg number impact on MTC for the non porosity case. We have observed that the MTC is increasing function of Weissenberg number. For non-porosity assumption, the MTC holds higher magnitude as compared to porous surface.

The neural networking modeling are used to make prediction and decisions in various fields. Particularly in the field of fluid science the neural networking models [37–41] can be used for prediction of flow field parameters. To anticipate the Sherwood number, we employed five inputs: the porosity, the Schmidt number, the magnetic field, Weissenberg number and the chemical reaction parameter. The first layer includes these inputs, and intermediate layer comprises 10 neurons. The

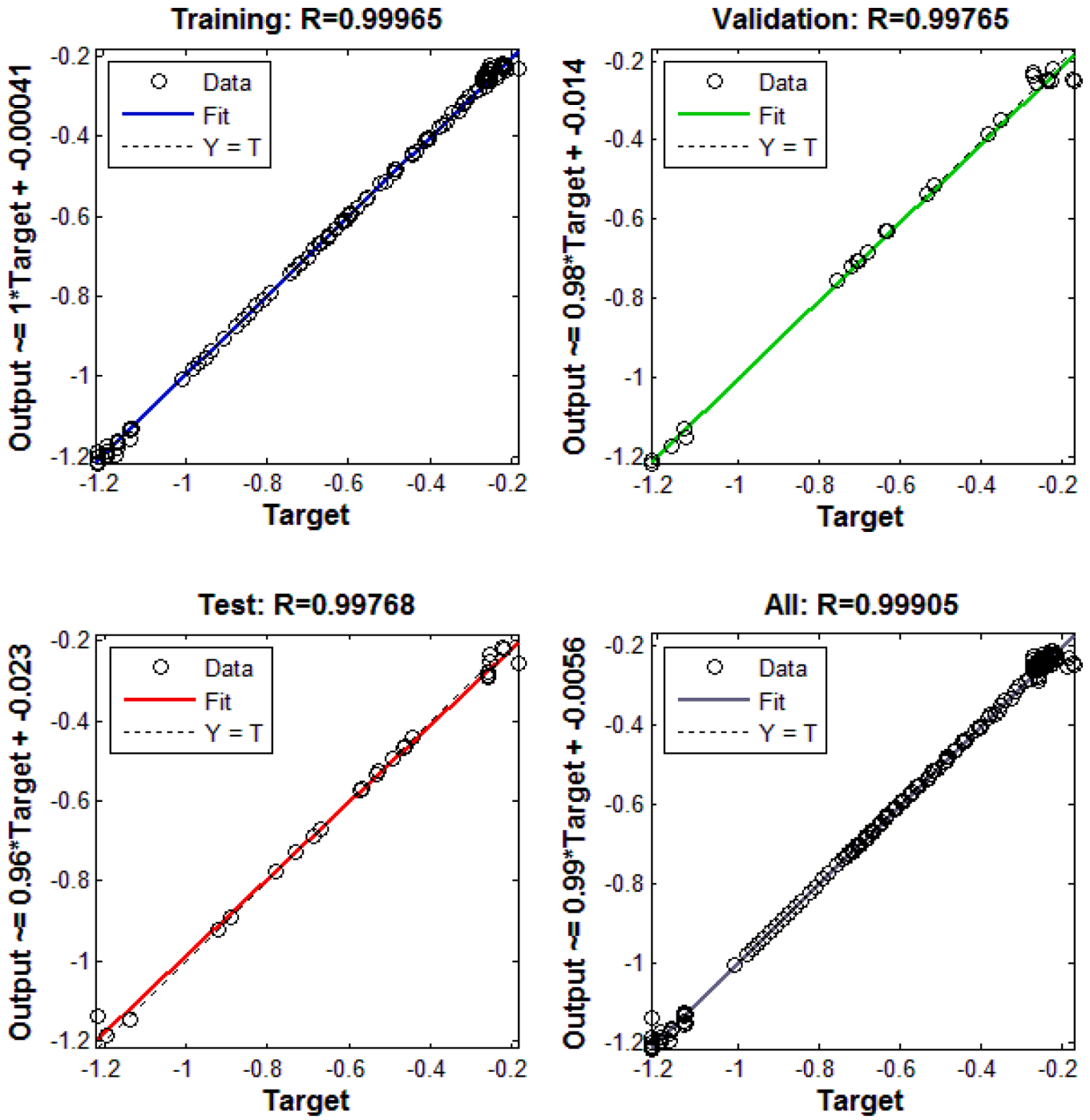

Fig. 6. Regression plot for constructed model.

last layer includes the ShD as an output. This is depicted graphically in Fig. 1(c). The Sigmoid function is utilized as a transfer function in the hidden layer, whereas in last layer Purelin function is used. The relationships for functions are:

$$F_a(X_c) = \frac{1}{1+e^{-X_c}}, \qquad \text{purelin}(X_c) = X_c. \tag{37}$$

Both MSE and R are used to measure the performance of constructed neural networking model. The expression are as follows:

$$\text{MSE} = \frac{1}{K}\sum_{q=1}^{K}\left(X_{\text{T(q)}} - X_{\text{P(q)}}\right)^2,$$

$$\text{R} = \sqrt{1 - \frac{\sum_{q=1}^{K}\left(X_{\text{T(q)}} - X_{\text{P(q)}}\right)^2}{\sum_{q=1}^{K}\left(X_{\text{T(q)}}\right)^2}}. \tag{38}$$

The porosity, Schmidt number, magnetic, Weissenberg number, and chemical reaction parameters are considered as an input to get 164 sample values of Sherwood number. The 164 ShD values are divided randomly into three models: training, validation, and testing. The 114

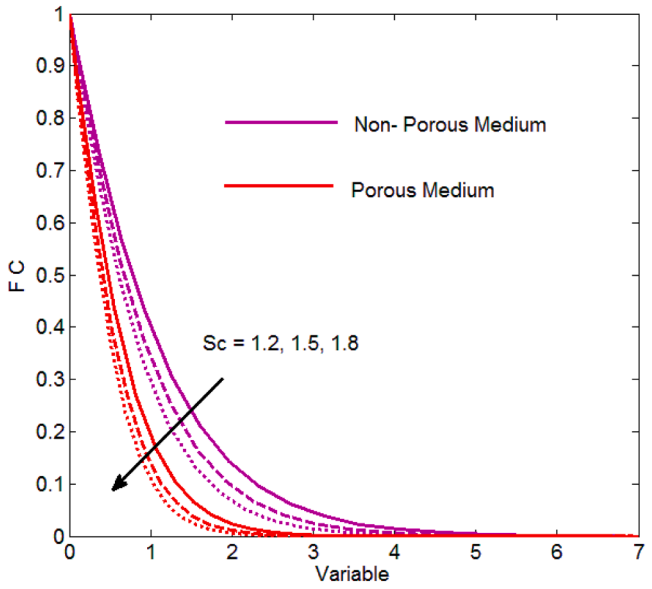

Fig. 7. FC for Sc number.

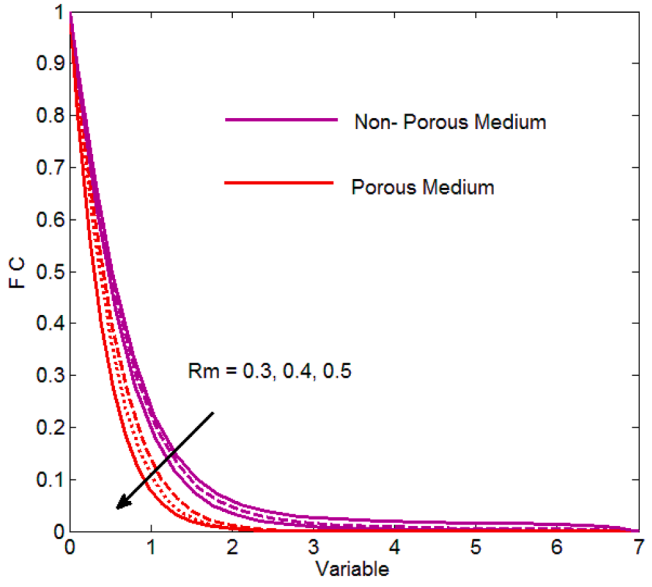

Fig. 8. FC for Rm parameter.

Table 9
Comparative study with Fathizadeh et al. [42].

Flow Variable	Fathizadeh et al. [42]	Present Study
M_c	Exact Data	Shooting Data
0.0	−1.0000	−1.0000
1.0	−1.41421	−1.4142
5.0	−2.44948	−2.4494
10	−3.31662	−3.3166
50	−7.14142	−7.1414

values, which account for 70 % of the total, are allocated for training, while the 25 values, which account for 15 % of the total, are marked for validation and testing. Ten neurons are chosen in the middle layer. Using the Levenberg-Marquardt approach, the network is trained to predict ShD. When processing nonlinear systems, the Levenberg-Marquardt algorithm works well because it has superior anti-interference and tracking capabilities than other control strategies.

The results of the ANN development to forecast the ShD are shown in Figs. 2–6. Fig. 2 depicts the performance of the ANN model in predicting ShD in greater detail.

A histogram of error values is shown in Fig. 3. Fig. 4 depicts the discrepancy between predicted and intended ShD values visually. Fig. 5 offers a comparison of predicted and desired ShD values. Figs. 6 and 7 illustrate the regression findings. In detail, Fig. 2 depicts the performance plot in predicting ShD. The mean square error for validation, training, and testing drops to necessary values as the number of epochs increases. MSE error provided the best estimates for testing and training. The best validation performance at epoch 48 is 0.0006161. Fig. 3 depicts the error histogram for the developed ANN for forecasting the Sherwood number.

One can observe that error values between intended ShD and predicted ShD is rather low, indicating that the neural model was well trained. The error value for 164 sample data of Sherwood number is shown in Fig. 4. One can see that only a few values admit the error of 0.08, 0.06 and −0.04 while all other values hold errors between −0.02 and +0.02. The evaluation plot of predicted and targeted Sherwood number values is shown in Fig. 5. We noticed that the two values are fairly similar. As a consequence, when heat transmission, magnetic field, velocity slip, thermal slip, heat production, and chemical reaction aspects are present, the constructed ANN is the best for forecasting the Sherwood on a flat porous surface. Fig. 6 depicts the regression analysis based on the constructed ANN to anticipate the Sherwood number. Fig. 6 depicts the regression outcome for training, validation, testing, and all. According to Fig. 6, the value for training is R = 0.99965, whereas the values for testing and validation are R = 0.99765 and 0.99768, respectively. The entire value for training, validation, and testing is R = 0.99905. This means that the intended and expected Sherwood number values are strongly correlated.

The MSE for training, testing, and validation are respectively 8.98041e-05, 6.16098–04, and 5.43810e-04. According to these statistics, the built neural networking model is the best at predicting Sherwood number values for magnetic surfaces. Therefore, the constructed ANN model is the remedy to offer the solution of the Carreau flow field up to a wide range of flow parameters. Figs. 7 and 8 show the impact of the Schmidt number and chemical reaction on the concentration profile in porous and non-porous situations, respectively. The influence of Sc on the concentration profile is depicted in Fig. 7 for both assumptions namely porous and non-porous. We discovered that when Sc increases, so does the fluid concentration. On both surfaces, the impact is the same. It is implied that the momentum diffusivity is significantly greater than the mass diffusivity when the Schmidt number is high. The fluid in this instance can be characterized as "momentum-dominated." It indicates that the fluid momentum transfer capacity is far greater than its mass transport capacity. As a result, in relation to the fluid's motion, the solute concentration will diffuse more slowly. Lower mass transfer rates will arise from a thicker concentration boundary layer.

The concentration profile is stronger on non-porous surfaces. Fig. 8 depicts the concentration variation for a chemical reaction parameter. We determined that concentrations for both surfaces are decreased about the chemical reaction parameter. It is significant to remember that different elements, such as reaction kinetics, reaction mechanisms, transport processes, and boundary conditions, affect how a chemical reaction specifically affects fluid concentration. The magnitude of concentration is larger on non-porous surfaces than on porous surfaces. It can be noted that if we neglect velocity slip, porosity, mass and heat transfer aspects, then the present study reduces to the study reported by Fathizadeh et al. [42]. For comparison purpose, the skin friction coefficient is evaluated for magnetic field parameter. By following Table 9, we establish an excellent match that yields the validation of present outcomes.

5. Conclusion

Artificial intelligence analysis is performed with the assistance of Lie symmetry to examine the Carreau flow field when mass and heat transfer aspects are considered. The flow field is manifested with chemical reaction, thermal slip, heat generation, velocity slip, and magnetic field. The concentration and mass transfer rate are evaluated by a constructed neural networking model. The important findings are as follows:

- The MSE for training, testing, and validation are respectively 8.98041e-05, 6.16098–04, and 5.43810e-04.
- The entire value for validation, training, and testing is R = 0.99905 which reflects the strong correlation of targeted and predicted values.
- The predicted values by the neural networking model show that the Sherwood number is an increasing function of the chemical reaction parameter and Schmidt number.
- The Carreau concentration profile shows decline trends towards both the Schmidt number and chemical reaction parameter.
- For non-porous surface, the magnitude of Carreau concentration is noticed higher for positive variation in chemical reaction parameter and Schmidt number.
- The work can be extended to examine the Carreau fluid flow with mass transfer over curved surfaces. This could provide information about how these findings might be used in real-world industrial processes like coating and pipe flows.

CRediT authorship contribution statement

Khalil Ur Rehman: Writing – original draft, Methodology, Investigation, Formal analysis, Data curation, Conceptualization. **Wasfi Shatanawi:** Validation, Supervision, Methodology, Investigation. **Zeeshan Asghar:** Writing – original draft, Visualization, Software, Investigation. **A.R.M. Kasim:** Investigation, Formal analysis, Data curation, Conceptualization.

Declaration of competing interest

Authors have no conflict of Interest at this stage.

Acknowledgment

This work was supported by a Seed Project research grant from Prince Sultan University, Saudi Arabia (SEED-CHS-2024-{169}).

Data availability

Data will be made available on request.

References

[1] Ivan Machač, Bedřich Šiška, Ludmila Machačová, Terminal falling velocity of spherical particles moving through a Carreau model fluid, Chem. Eng. Process.: Process Intensif. 39 (4) (2000) 365–369.
[2] K. Khellaf, G. Lauriat, Numerical study of heat transfer in a non-Newtonian Carreau-fluid between rotating concentric vertical cylinders, J. Non-Newton. Fluid Mech. 89 (1–2) (2000) 45–61.
[3] Ivan Machač, Bedřich Šiška, Roman Teichman, Fall of non-spherical particles in a Carreau model liquid, Chem. Eng. Process.: Process Intensif. 41 (7) (2002) 577–584.
[4] Jyh-Ping Hsu, Shih-Hsing Hung, Hsiu-Yu Yu, Electrophoresis of a sphere at an arbitrary position in a spherical cavity filled with Carreau fluid, J. Colloid Interface Sci. 280 (1) (2004) 256–263.
[5] Eric Lee, Chi-Tien Chen, Jyh-Ping Hsu, Electrophoresis of a rigid sphere in a Carreau fluid normal to a planar surface, J. Colloid Interface Sci. 285 (2) (2005) 857–864.
[6] Bedřich Šiška, Helena Bendová, Ivan Machač, Terminal velocity of non-spherical particles falling through a Carreau model liquid, Chem. Eng. Process.: Process Intensif. 44 (12) (2005) 1312–1319.
[7] Jyh-Ping Hsu, Wei-Jyh Chen, Shiojenn Tseng, Chur-Jen Chen, Sedimentation of a cylindrical particle along the axis of a cylindrical tube filled with Carreau fluid, Powder Technol. 166 (1) (2006) 1–13.
[8] Nasir Ali, Tasawar Hayat, Peristaltic motion of a Carreau fluid in an asymmetric channel, Appl. Math. Comput. 193 (2) (2007) 535–552.
[9] J.P. Hsu, S.J. Yeh, S. Tseng, Drag on a sphere in a spherical dispersion containing Carreau fluid, Powder Technol. 188 (1) (2008) 34–41.
[10] A. Shamekhi, K. Sadeghy, Cavity flow simulation of Carreau–Yasuda non-Newtonian fluids using PIM meshfree method, Appl. Math. Model. 33 (11) (2009) 4131–4145.
[11] T. Hayat, Najma Saleem, N. Ali, Effect of induced magnetic field on peristaltic transport of a Carreau fluid, Commun. Nonlinear Sci. Numer. Simul. 15 (9) (2010) 2407–2423.
[12] E. De la Guerra Ochoa, J. Echavarri Otero, E. Chacón Tanarro, P. Lafont Morgado, A. Diaz Lantada, Juan Manuel Munoz-Guijosa, J.L. Muñoz Sanz, New Reynolds equation for line contact based on the Carreau model modification by Bair, Tribol. Int. 55 (2012) 141–147.
[13] Yabin Shao, An Wu, S.Z. Abbas, W.A. Khan, I.M. Ashraf, Thermal management for the shear-rate driven flow of Carreau fluid in a ciliated channel, Int. Commun. Heat Mass Transf. 139 (2022) 106473.
[14] Kudenatti, Ramesh B., Noor E. Misbah, and M.C. Bharathi. "A numerical study on boundary layer flow of Carreau fluid and forced convection heat transfer with viscous dissipation and generalized thermal conductivity." *Math. Comput. Simul.* 208 (2023): 619–636.
[15] Anuar Ishak, Roslinda Nazar, Norfifah Bachok, Ioan Pop, MHD mixed convection flow adjacent to a vertical plate with prescribed surface temperature, Int. J. Heat Mass Transf. 53 (21–22) (2010) 4506–4510.
[16] Turkyilmazoglu, Mustafa. "MHD fluid flow and heat transfer due to a stretching rotating disk." *Int. J. Therm. Sci.* 51 (2012): 195–201.
[17] Md Nasir Uddin, M.A. Alim, M.M.K. Chowdhury, Effects of mass transfer on MHD mixed convective flow along inclined porous plate, Procedia Eng. 90 (2014) 491–496.
[18] Srikanth, G.V.P.N., G. Srinivas, and B.Suresh Babu. "Characterization of chemical reaction on heat transfer through the nano fluid." *Procedia Mater. Sci.* 10 (2015): 10–18.
[19] Z. Abbas, M. Sheikh, S.S. Motsa, Numerical solution of binary chemical reaction on stagnation point flow of Casson fluid over a stretching/shrinking sheet with thermal radiation, Energy 95 (2016) 12–20.
[20] Kumar, K.Ganesh, N.G. Rudraswamy, and B.J. Gireesha. "Effects of mass transfer on MHD three dimensional flow of a Prandtl liquid over a flat plate in the presence of chemical reaction." *Results. Phys.* 7 (2017): 3465–3471.
[21] Krishna, M.Veera, and Kamboji Jyothi. "Hall effects on MHD rotating flow of a visco-elastic fluid through a porous medium over an infinite oscillating porous plate with heat source and chemical reaction." *Mater. Today: Proc.* 5, no. 1 (2018): 367–380.
[22] Dharmendar Reddy Yanala, Shankar Goud Bejawada, Kottakkaran Sooppy Nisar, Influence of Chemical reaction and heat generation/absorption on Unsteady magneto Casson Nanofluid flow past a non-linear stretching Riga plate with radiation, Case Stud. Therm. Eng. 50 (2023) 103494.
[23] Pooja Agarwal, K. Loganathan, Reema Jain, Entropy optimization of chemically reactive bioconvective Powell-Eyring nanofluid stratified flow over a Riga plate: a non-Fourier heat and mass flux modeling, Partial Differ. Equ. Appl. Math. 9 (2024) 100616.
[24] M. Khan, M. Irfan, W.A. Khan, A.S. Alshomrani, A new modeling for 3D Carreau fluid flow considering nonlinear thermal radiation, Results. Phys. 7 (2017) 2692–2704.
[25] Eid, Mohamed R., Kasseb L. Mahny, Taseer Muhammad, and Mohsen Sheikholeslami. "Numerical treatment for Carreau nanofluid flow over a porous nonlinear stretching surface." *Results. Phys.* 8 (2018): 1185–1193.
[26] Mair Khan, Arif Hussain, M.Y. Malik, T. Salahuddin, Shaban Aly, Numerical analysis of Carreau fluid flow for generalized Fourier's and Fick's laws, Appl. Numer. Math. 144 (2019) 100–117.
[27] Muhammad Bilal, Anwar Saeed, Taza Gul, Muhammad Rehman, Amir Khan, Thin-film flow of Carreau fluid over a stretching surface including the couple stress and uniform magnetic field, Partial Differ. Equ. Appl. Math. 4 (2021) 100162.
[28] Muhammad Rooman, Zahir Shah, Ebenezer Bonyah, Muhammad Asif Jan, Wejdan Deebani, Mathematical modeling of Carreau fluid flow and heat transfer characteristics in the renal tubule, J. Math. 2022 (2022) 1–14.
[29] Zakir Ullah, Gul Zaman, Lie group analysis of magnetohydrodynamic tangent hyperbolic fluid flow towards a stretching sheet with slip conditions, Heliyon. 3 (11) (2017).
[30] K.Ur Rehman, Wasfi Shatanawi, Kamaleldin Abodayeh, Thermophysical aspects of magnetized Williamson fluid flow subject to both porous and non-porous surfaces: a Lie symmetry analysis, Case Stud. Therm. Eng. 28 (2021) 101688.
[31] Anum Shafiq, Andaç Batur Çolak, Tabassum Naz Sindhu, Analyzing activation energy and binary chemical reaction effects with artificial intelligence approach in axisymmetric flow of third grade nanofluid subject to Soret and Dufour effects, Heat Transf. Res. 54 (3) (2023).
[32] Yasir Nawaz, Muhammad Shoaib Arif, Kamaleldin Abodayeh, Atif Hassan Soori, A two-stage multi-step numerical scheme for mixed convective Williamson nanofluid flow over flat and oscillatory sheets, Int. J. Mod. Phys. B 38 (22) (2024) 2450298.
[33] Subhan Ullah, Ikram Ullah, Amir Ali, Kamal Shah, Thabet Abdeljawad, Investigation of cross-diffusion effect on radiative Jeffery-Hamel flow in convergent/divergent stretchable channel with Lorentz force and Joule heating, Alex. Eng. J. 86 (2024) 289–297.

[34] S. Manjunatha, K.U. Rehman, J. Santhosh Kumar, S.V.K. Varma, W. Shatanawi, On thermal non-equilibrium (TNE) model for heat transfer in ternary ferro-nanofluid with rectangular porous fin, Int. J. Thermofluids. 23 (2024) 100757.
[35] Khursheed Muhammad, Shaimaa AM Abdelmohsen, Ashraf MM Abdelbacki, B. Ahmed, Darcy-Forchheimer flow of hybrid nanofluid subject to melting heat: a comparative numerical study via shooting method, Int. Commun. Heat Mass Transf. 135 (2022) 106160.
[36] K.Ur Rehman, Wasfi Shatanawi, Uroosa Firdous, A comparative thermal case study on thermophysical aspects in thermally magnetized flow regime with variable thermal conductivity, Case Stud. Therm. Eng. 44 (2023) 102839.
[37] Shafiq, Anum, Andaç Batur Çolak, Tabassum Naz Sindhu, Qasem M. Al-Mdallal, and T. Abdeljawad. "Estimation of unsteady hydromagnetic Williamson fluid flow in a radiative surface through numerical and artificial neural network modeling." *Sci. Rep.* 11, no. 1 (2021): 14509.
[38] S. Bilal, Muhammad Bilal Riaz, Thermofluidic transport of Williamson flow in stratified medium with radiative energy and heat source aspects by machine learning paradigm, Int. J. Therm. 24 (2024) 100818.
[39] O.M. Amoo, A. Ajiboye, M.O. Oyewola, Analysis of thermophysical and transport properties of nanofluids using machine learning algorithms, Int. J. Therm. 21 (2024) 100566.
[40] Anum Shafiq, Andaç Batur Çolak, Tabassum Naz Sindhu, Comparative analysis to study the Darcy–Forchheimer Tangent hyperbolic flow towards cylindrical surface using artificial neural network: an application to Parabolic Trough Solar Collector, Math. Comput. Simul. 216 (2024) 213–230.
[41] K.U. Rehman, W. Shatanawi, Taqi AM Shatnawi, Lie symmetry neural networking for heat transfer in magnetized williamson fluid (MWF) with heat source (HS) and thermal slip (TS), Int. J. Therm. 24 (2024) 100870.
[42] M. Fathizadeh, M. Madani, Yasir Khan, Naeem Faraz, Ahmet Yıldırım, Serap Tutkun, An effective modification of the homotopy perturbation method for MHD viscous flow over a stretching sheet, J. King Saud Univ. Sci. 25 (2) (2013) 107–113.